Editors' Suggestion

Nanosecond rf-Power Switch for Gyrotron-Driven Millimeter-Wave Accelerators

S.V. Kutsaev,[1,*] B. Jacobson,[2,†] A.Yu. Smirnov,[1] T. Campese,[1] V.A. Dolgashev,[2] V. Goncharik,[3] M. Harrison,[1] A. Murokh,[1] E. Nanni,[2] J. Picard,[4] M. Ruelas,[1] and S.C. Schaub[4]

[1]*RadiaBeam Technologies LLC, 1717 Stewart St, Santa Monica, California 90403, USA*
[2]*SLAC National Accelerator Laboratory, 2575 Sand Hill Rd, Menlo Park, California 94025, USA*
[3]*Logicware Inc, New York, New York 11235, USA*
[4]*Massachusetts Institute of Technology, 77 Massachusetts Ave, Cambridge, Massachusetts 02139, USA*

(Received 9 October 2018; revised manuscript received 12 February 2019; published 21 March 2019)

The development of alternative mm-wave high-gradient, >200 MV/m, accelerating structures offers a promising path to reduce the cost and footprint of future TeV-scale linear colliders, as well as linacs for industrial, medical, and security applications. The major factor limiting accelerating gradient is vacuum rf breakdown. The probability of such breakdowns increases with pulse length. For reliable operation, millimeter-wave structures require nanoseconds-long pulses at the megawatt level. This power is available from gyrotrons, which have a minimum pulse length on the order of microseconds. To create shorter pulses and to reliably detect rf breakdowns, we developed the following devices: a laser-based rf switch capable of selecting 10 ns long pulses out of the microseconds long gyrotron pulses, thus enabling the use of the gyrotrons as power sources for mm-wave high-gradient linacs, and a shot-to-shot sub-THz spectrometer with high-frequency resolution, capable of detecting pulse shortening due to rf breakdowns.
We will describe the principle of operation of these devices and their achieved parameters. We also report on the experimental demonstration of these devices with the high-power gyrotron at the Massachusetts Institute of Technology. In the experiments, we demonstrate nanosecond rf power modulation, shot-to-shot measurements of the pulse spectra, and detection of rf breakdowns.

DOI: 10.1103/PhysRevApplied.11.034052

I. INTRODUCTION

The development of alternative high-gradient accelerating structures operating at THz frequencies is critical for future free-electron lasers [1] and TeV-scale linear colliders [2]. These facilities will open new horizons in chemical [3] and biological imaging [4], and high energy physics [5]. The demand to reach high energies within a reasonable length requires high accelerating gradients beyond 100 MV/m [6].

Recently, there has been a significant effort at SLAC National Accelerator Laboratory to push the operating frequency of linacs into the *W* band and beyond, with beam-driven 100- and 200-GHz accelerating structures [7,8], and gyrotron-driven 100- and 300-GHz structures [9,10]. These metal structures are made of two halves. The cavities are symmetrically milled into flat sides of metal blocks. When the two halves are placed together, they form an accelerating structure.

To reach high gradients, such structures require MW-level rf power. Experiments with beam-driven structures have shown that at these power levels, the rf pulses should be shorter than a few nanoseconds [11] for breakdown-free operation. Currently, the power sources capable of producing the megawatt power levels in this frequency range are gyrotrons, which generate microsecond-long pulses [12]. Therefore, gyrotron pulses have to be shortened in order to be fed into accelerating structures. We describe a laser-based rf switch capable of selecting a several-nanoseconds-long portion of a few-microseconds-long 1.5-MW 110-GHz pulse.

Vacuum rf breakdowns limit the working power and produce irreversible surface damage in high-power rf components, including accelerating cavities and sources [13]. They cause pulse shortening of the transmitted rf pulse, which results in a broadening of its spectrum. This spectrum broadening can be detected with a frequency spectrometer. Therefore, to commission the rf switch and reliably detect breakdowns in accelerating structures, we develop a shot-to-shot sub-THz spectrometer with high-frequency resolution.

II. RF SWITCH DESIGN

In order to selectively shorten the long pulse generated by the gyrotron, it is possible to implement light-controlled

*kutsaev@radiabeam.com
†Work performed while at RadiaBeam Technologies, Santa Monica, California 90404, USA

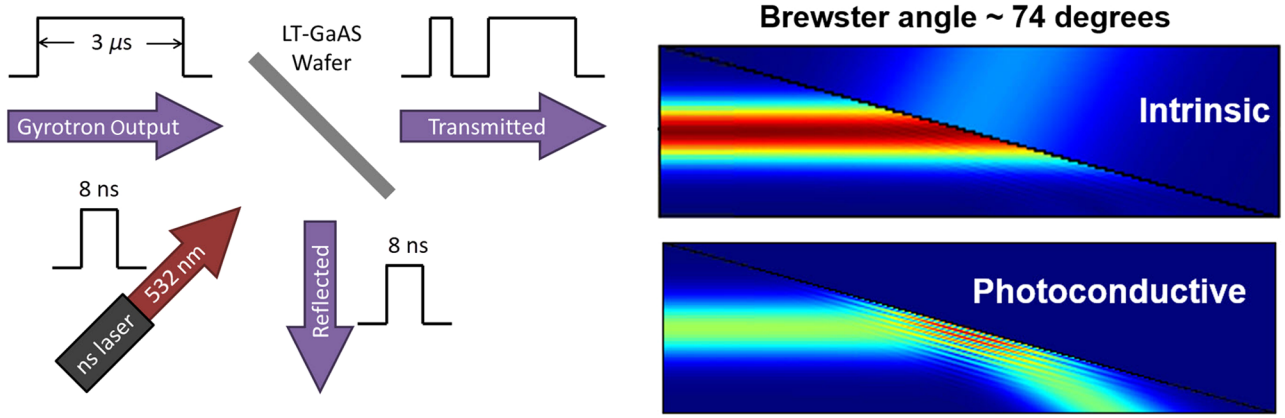

FIG. 1. Simplified geometry (left) and Brewster angle incidence (right) configurations of gated window. COMSOL multiphysics simulation results show the transmission (top right) of 100 GHz through the intrinsic semiconductor and reflection (bottom right) from the interface in the photoconductive state.

semiconductor shutters [14,15] via the photoconductive effect. While it is known that typical dielectric materials are transparent to microwaves, rf radiation reflects from metallic interfaces. In the case of semiconductors, which behave similarly to metals through the generation of free carriers from irradiation by light with photon energies above the material's band gap [16], both transparent and reflective states can be realized. Therefore, if illuminated by a short laser pulse, the two states of the semiconductor operate as a photogated switch for microwaves.

This principle of operation is depicted in Fig. 1, left. A long microwave pulse is incident on a semiconductor wafer. Illumination by a short laser pulse stimulates the photoconductive state of the wafer, picking out and reflecting a short rf pulse as output for device testing. After the laser pulse is off, the wafer returns to the intrinsic state and transmits the remainder of the microwave pulse.

COMSOL simulations of a 110-GHz wave interacting with the photoconductive state of the wafer exhibiting high reflectivity are shown in the bottom right of Fig. 1. In this model, the low conductivity of the GaAs intrinsic state is assigned a conductivity of 1360 S/m, which corresponds to a photoinduced carrier concentration of $N = 10^{22}$ m^{-3}.

The refractive index ($n \approx 3.6$ for GaAs) of the semiconductor in the intrinsic state causes some unwanted reflection of the incoming THz wave. To eliminate any power in the reflected beam when the laser is off that could be delivered to the structure under test, we exploit Brewster angle incidence [17]. For a polarized source incident at the Brewster angle, the reflected power is zero in the intrinsic state, as shown in the top right panel of Fig. 1. In testing, the Brewster angle for each wafer is altered to account for the different index of the particular material.

A. Surface plasma model of free charge carriers

Free charge carriers in materials distribute due to electrostatic forces, finding equilibrium arranged in a thin plasmalike layer at the material surface. The interaction of this surface plasma with an em wave can be modeled as a media of a frequency dependent complex index of refraction. A plasma frequency ω_p related to the charge carrier density, N, can be defined as: $\omega_p^2 = Ne^2/\epsilon_0 m^*$ where e is the universal charge quanta, ϵ_0 is the permittivity of free space, and m^* is the effective mass of the charge. In such a plasma, the frequency dependence of the relative dielectric function is given by: $\epsilon(\omega) = 1 - (\omega_p^2/\omega^2)$. When $\omega < \omega_p$, ϵ becomes negative, the index of refraction becomes complex, and only higher frequencies propagate through the plasma.

In the semiconductor intrinsic state, GaAs has a carrier density of $N_{\text{intr}} \sim 10^{12}$ m^{-3}. The plasma frequency in this state corresponds to approximately 35 MHz; 110-GHz waves freely propagate through the surface. Stimulating the photoconductive state increases the carrier concentration by orders of magnitude. At a carrier concentration of $N_{\text{phot}} \sim 10^{19}$ m^{-3}, the plasma frequency is 110 GHz. At higher carrier densities, the wafer will begin to reflect the gyrotron power.

B. Photon absorption and carrier generation

A simple model of photon absorption and carrier production in the semiconductor is used: every photon absorbed generates one electron-hole pair and the charge generation rate, g, is the same as the photon absorption rate. The absorption of light leads to attenuation following Beer's law: $I(x) = I_0 \exp(-\alpha x)$ where I_0 is the optical power flux (in W/m^2) incident at the surface, x is the penetration depth into the wafer, and α is the frequency dependent linear absorption coefficient [18]. The exponential decay of Beer's law implies that the majority of the optical power is absorbed in a layer of material $d = 1/\alpha$ thick. For example, at 532 nm, the absorption coefficient in GaAs is $\alpha = 7.9 \times 10^4$ cm^{-1} and the photons are absorbed in a

thin layer $d \sim 0.1\ \mu$m. However, at 110 GHz, far below the conduction band-gap energy, the absorption coefficient is $\alpha \sim 0.4\ \text{cm}^{-1}$ and $d \sim 2.5$ cm. At this frequency, there is almost no attenuation through a sub-mm-thick wafer.

In order to estimate the charge carrier density generated, consider illumination by a uniform plane wave with a power flux I_0 (W/m^2) and the photon absorption within a layer $d = 1/\alpha$. To calculate the photon density within this layer, the power flux is averaged as it is attenuated from the surface to the bottom of the layer. The average intensity is $I_{\text{ave}} = 0.63\ I_0$. For this estimation, we assume that the photon absorption is uniformly distributed throughout the volume of the thin surface layer and generates a uniform charge density equal to the number of photons in this volume.

The charge carrier density generation rate g, measured in SI units of $\text{s}^{-1}\ \text{m}^{-3}$, is then $g = I_{\text{ave}}/(E_\gamma d)$, where E_γ is the energy of the absorbed photon. During illumination, an equilibrium between charge carrier generation and recombination is reached. The increase in charge density during this photoconductive steady state is $\delta N = g\tau$, where τ is the recombination time, or in terms of illumination and material parameters

$$\delta N = \frac{0.63\ \ I_0 \alpha \tau}{E_\gamma}. \tag{1}$$

However, once the illuminating pulse turns off, charge generation ceases and carriers are removed from the conduction band through recombination. The time scale for the charge density, N, to exponentially decay and return to the intrinsic state, thus turning off the laser-induced microwave reflectivity, is the recombination time τ. GaAs has a fast ($\tau_{\text{GaAs}} \sim 10$ ns) recombination time, which is comparable to the required pulse lengths [19] and is a good match for this application. We also test an undoped Si wafer, which has a recombination time of $\tau_{\text{Si}} \sim 1\ \mu$s, producing a reflectivity that decays 100 times more slowly, as shown in our measurements in Fig. 10.

C. Drude-Lorentz model of complex dielectric function in photoconductive state

The simple plasma model of the dielectric function's frequency dependence provides an intuitive insight of the behavior of semiconductors in the photoconductive state, however, it does not account for interactions among the conduction band charge carriers. The Lorentz oscillator equation is a more general model, which includes the physical interactions between bulk electrons (polarization) and the incident electric field (through the ω_p term), damping caused by charge carrier collisions (the Γ term), and a line resonance (the ω_0 term). Here, ϵ_∞ is a real constant representing the high-frequency asymptotic limit and the dielectric function is complex, $\epsilon = \epsilon' + i\epsilon''$

$$\epsilon(\omega) = \epsilon_\infty + \frac{\omega_p^2}{\omega_0^2 - \omega^2 + i\omega\Gamma}.$$

This relation can be further simplified in the case of metals and can be analyzed using a modified form, the Drude-Lorentz model of permittivity [20], where the line resonance is set to dc since electrons in the conduction band do not experience the restoring force felt by electrons in bound states. This is also true for photogenerated electron-hole pairs excited to the conduction band in semiconductors. The damping coefficient corresponds to the carrier collision time, $\Gamma = 2\pi/\tau_{\text{col}}$, which is related to the carrier mobility μ and effective mass m^* by $\tau_{\text{col}} = \mu m^*/e$. The collision time is much shorter than the recombination time, in GaAs $\tau_{\text{col}} \sim 0.3$ ps and in Si $\tau_{\text{col}} \sim 0.1$ ps, and is different from the recombination time, τ, relating the charge generation rate to the induced carrier density, $\delta N = g\tau$, in the photoconductive steady state. With these substitutions, the real and imaginary dielectric functions are given by

$$\epsilon'(N,\omega) = \epsilon_\infty - \frac{\frac{Ne^2 m^*}{\epsilon_0}}{(m^*\omega)^2 + \left(\frac{2\pi e}{\mu}\right)^2}, \tag{2}$$

and

$$\epsilon''(N,\omega) = \frac{\frac{2\pi N e^3}{\mu \epsilon_0}}{(m^*)^2\omega^3 + \omega\left(\frac{2\pi e}{\mu}\right)^2}. \tag{3}$$

D. Estimation of switch illumination power requirements

The complex refractive index, $\tilde{n} = n + ik$, can be computed as a function of carrier concentration and frequency using the Drude-Lorentz model dielectric function, and the physical properties (effective mass and mobility) of a particular semiconductor material. The real (n) and imaginary (k) components of the complex refractive index are related to the dielectric function $\epsilon(N,\omega)$ by $n(N,\omega) = \sqrt{(|\epsilon| + \epsilon')/2}$ and $k(N,\omega) = \sqrt{(|\epsilon| - \epsilon')/2}$.

The fraction of microwave reflected power can be computed from the complex refractive index by writing the ansatz $n \to \tilde{n}(N,\omega)$ in the Fresnel equation for the electric field reflectivity coefficient. The expression for the power reflection coefficient of p polarized waves traveling in air (angle of incidence θ_i, and angle of transmission θ_t) from the semiconductor is

$$R = r_p r_p^* = \frac{(n^2+k^2)\cos^2\theta_i - 2n\ \cos\theta_i \cos\theta_t + \cos^2\theta_t}{(n^2+k^2)\cos^2\theta_i + 2n\ \cos\theta_i \cos\theta_t + \cos^2\theta_t}. \tag{4}$$

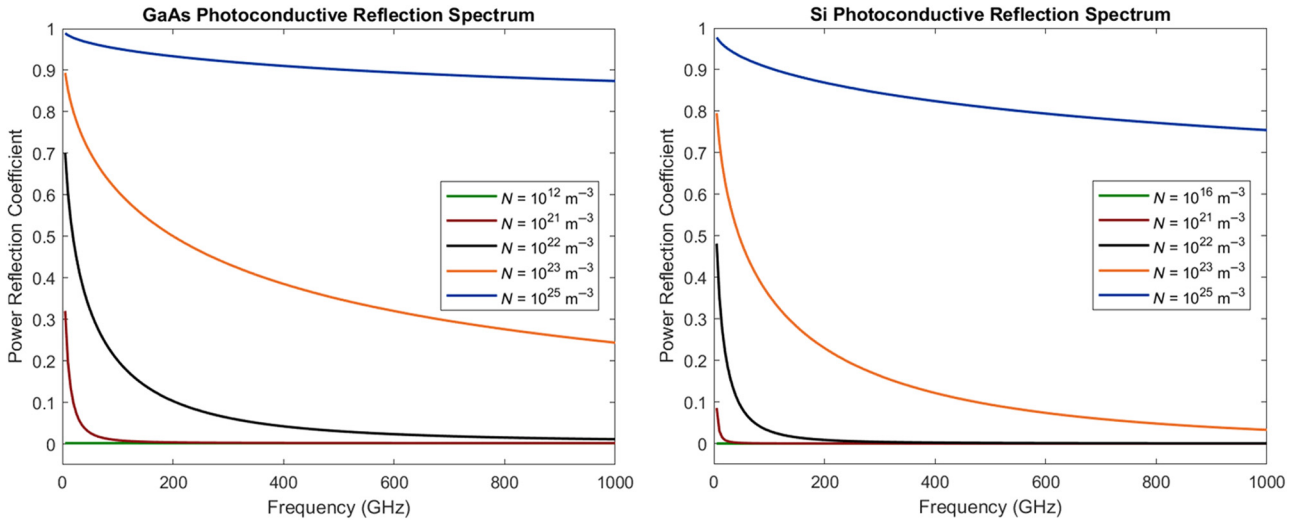

FIG. 2. Power reflection coefficient for GaAs (left) and Si (right) as a function of frequency for various carrier concentrations from intrinsic state (10^{12} m^{-3} in GaAs and 10^{16} m^{-3} in Si) to a highly photoconductive state 10^{25} m^{-3}.

The reflected power coefficients are plotted as a function of frequency up to 1 THz in Fig. 2 for carrier concentrations that increase from the semiconductor intrinsic state (without illumination) to highly photoconductive charge densities. In all cases, the rf wave is incident at Brewster's angle, calculated from values widely accepted in the literature, which are appropriate for 110 GHz. The geometry used in this analysis is fixed for each material: for GaAs, $\theta_i = 74.4^\circ$ and $\theta_t = 15.6^\circ$; for Si, $\theta_i = 73.7^\circ$ and $\theta_t = 16.3^\circ$. The plots show that at the highest charge density considered the power reflection coefficient exceeds 90% at 110 GHz for each material.

The angular dependence of the reflectivity for increasing charge concentrations is also modeled. Using the same ansatz, $n \to \tilde{n}(N, \omega)$, a modified Snell's law recasts the reflected power coefficient as a function of θ_i

$$R = r_p r_p^* = \frac{(n^2+k^2)\cos^2\theta_i - 2n\cos\theta_i\sqrt{1-\frac{\sin^2\theta_i}{n^2+k^2}} + 1 - \frac{\sin^2\theta_i}{n^2+k^2}}{(n^2+k^2)\cos^2\theta_i + 2n\cos\theta_i\sqrt{1-\frac{\sin^2\theta_i}{n^2+k^2}} + 1 - \frac{\sin^2\theta_i}{n^2+k^2}}. \tag{5}$$

The power reflection coefficient for various charge densities and evaluated at 110 GHz is plotted in Fig. 3 as a function of θ_i. As the charge carrier concentration rises, the minimum in the power reflection coefficient curve shifts higher, toward glancing incidence, and becomes nonzero, eliminating the Brewster's effect. There are

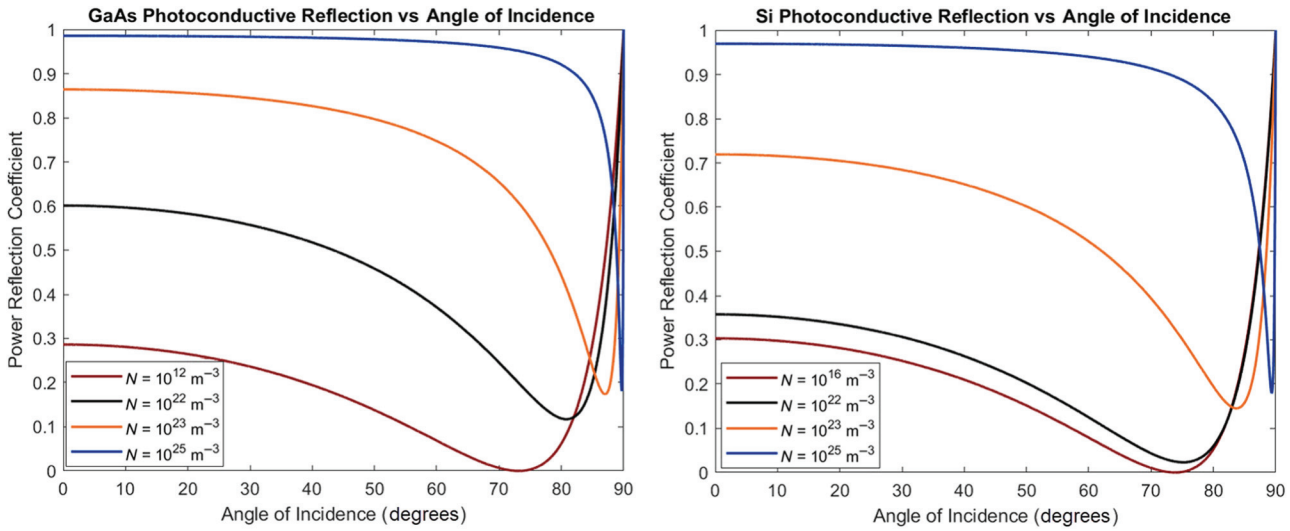

FIG. 3. Power reflection coefficient evaluated at 110 GHz for GaAs (left) and Si (right) as functions of incidence angle for various carrier concentrations from intrinsic state (10^{12} m^{-3} in GaAs and 10^{16} m^{-3} in Si) to a highly photoconductive state 10^{25} m^{-3}.

differences between the performance of the two materials at intermediate values of N, GaAs being more responsive to increased concentrations. In the highly photoconductive state, for $N = 10^{25}$ m^{-3} in either material, the reflectivity profile becomes flat for all but very steep angles and $R \geq 0.9$ for incidence at Brewster's angle.

Finally, we consider the case again with the rf incident upon the wafer fixed in the Brewster's angle configuration and now for the frequency of interest in this application, $f = 110$ GHz. The power reflection coefficients for GaAs and Si are plotted in the left panel of Fig. 4 using Eq. (4) for fixed frequency and angles as a function of the carrier concentration density. Again, the plot shows reflection coefficients exceeding 90% at $N = 10^{25}$ m^{-1} in each material. This analysis also agrees with the previous two cases examining frequency and angular dependencies in that, for a given charge concentration, the GaAs material outperforms Si given that the photoinduced reflectivity is greater for the same charge concentration. Examination of Fig. 4 (left) shows a horizontal shift between the two curves by roughly a factor of approximately 4.

The photoinduced charge density is converted by Eq. (1) to a corresponding illumination intensity and is plotted in the right panel of Fig. 4. It is notable that when plotted vs intensity, the Si wafer outperforms GaAs by a factor of approximately 2.5. Taking the ratio of Eq. (1) for GaAs to Si reveals that almost 9 times the intensity is required for GaAs to generate the same charge density generated in Si. This explains the responsivity change: $9 \div 4 = 2.25 \cong 2.5$, which is the intensity Si light-to-charge generating overperformance divided by the Si charge-to-reflectivity underperformance. In terms of intensity, the 90% threshold for the power reflection coefficient occurs when the wafer is illuminated by green 532-nm laser light of intensity 8 MW/m^2 for Si and by 20 MW/m^2 for GaAs.

E. Laser-driven rf switch prototype for high-power bench test and evaluation

We design and construct an enclosed tabletop version of the rf switching apparatus for the high-power experiment as shown in Fig. 5. The 110-GHz radiation enters from the input window at the top, propagating down through the polarizer and Teflon THz lens. At the wafer, the THz pulse is switched; the long pulse enters the power dump and the short pulse is reflected by the wafer toward the gold mirror through the Teflon focusing lenses. This output pulse exits through the window for delivery to the device under test.

The wafer is illuminated by a Quantas Q1B-1064-10 electro-optically Q switched diode-pumped Nd:YAG laser with second harmonic generation (SHG) unit. The SHG process produces 532-nm light in approximately 10-ns pulses with a maximum repetition rate of 10 Hz. The maximum pulse energy of the green beam is 5 mJ and corresponds to a peak power of roughly 500 kW, which, when (here assumed to be uniform) illuminating a 4-cm-diameter circle, produces an intensity of nearly 400 MW/m^2. The stimulated photocarrier density for this illumination intensity is calculated to be $N = 5 \times 10^{25}$ m^{-3} in GaAs, just above the maximum concentration plotted in Figs. 2 and 3. For both GaAs and Si switches in this highly photoconductive state, the power reflection coefficient exceeds about 90% at 110 GHz. Gallium arsenide performs slightly better than silicon for a given switching illumination, as presented in Fig. 4. Characterizations

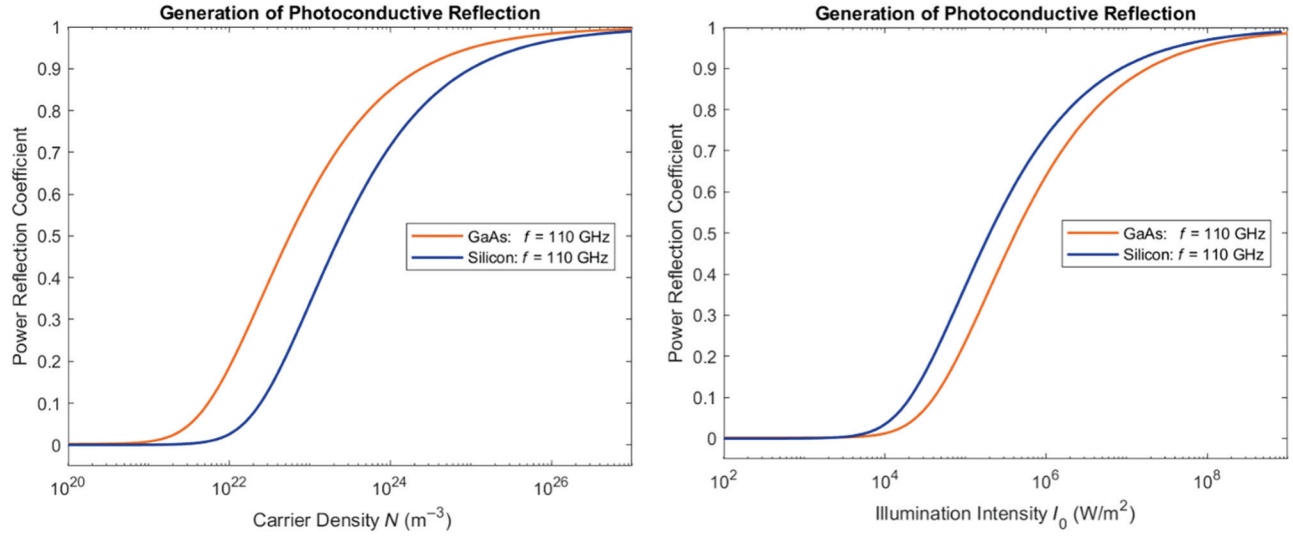

FIG. 4. Power reflection coefficient evaluated at 110 GHz for GaAs and Si as functions of carrier concentration (left) and laser illumination intensity (right) in the Brewster's angle configuration. Note the apparent switch in responsivity from left to right.

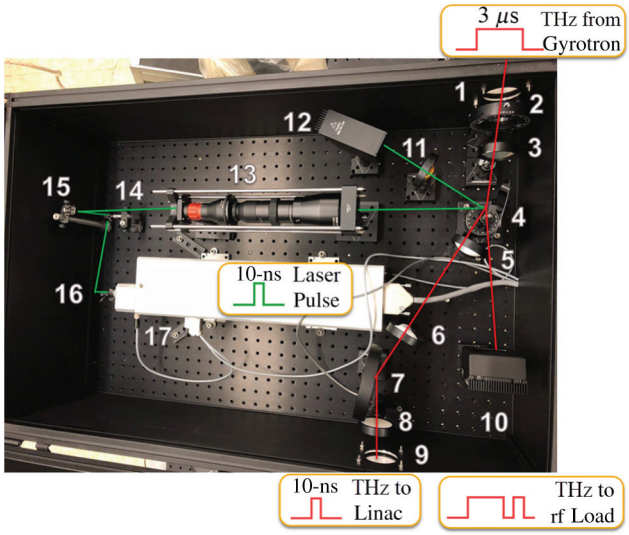

FIG. 5. Schematics of the laser-driven rf switch. 1 – Input THz window, 2 – Polarizer, 3 – THz lens no. 1, 4 – Wafer, 5 – THz lens no. 2, 6 – THz lens no. 3, 7 – Mirror, 8 – THz lens no. 4, 9 – Output THz window, 10 – THz load, 11 – Optical lens, 12 – Laser dump, 13 – Beam expander, 14 – Alignment mirror no. 1, 15 – Alignment mirror no. 2, 16 – Alignment mirror no. 3, 17 – 532 nm laser. Laser light is shown with green lines, THz signal with red lines.

of the system and high-power bench test are described below.

III. SHOT-TO-SHOT SPECTROMETER DESIGN

The idea of the superheterodyne spectrometer is to mix the input signal with a central frequency (f) and a signal from a local oscillator (LO) with a known frequency (f_0). The resulting signal will have a component frequency of ($\Delta f = |f - f_0|$), which can be digitized and then analyzed with Fourier analysis. The actual input signal spectrum can be obtained by simply adding the LO frequency. To solve the problem of the down-converted frequency ambiguity (below or above the LO frequency), a quadrature mixer can be used, which will produce two signals, shifted by 90°. The sign of the relative phase will indicate the sign of Δf. The frequency resolution of this method will be equal to $1/\Delta T$, where ΔT is the detected pulse length. Practically, for shorter pulses, we will measure wider spectra due to this effect, as shown in Fig. 6.

In the designed spectrometer, the down-conversion heterodyne is formed with an input horn antenna, 100–120-GHz band-pass WR-08 filter, 6-dB directional coupler, IQ-mixer, and a local oscillator with a fixed frequency of 110.08 GHz, corresponding to the MIT gyrotoron's frequency, as shown in Fig. 7. The design also incorporates a Schottky amplitude detector to visually observe the pulse shortening. The three signals (envelope, I, and Q) are then digitized and Fourier analyzed.

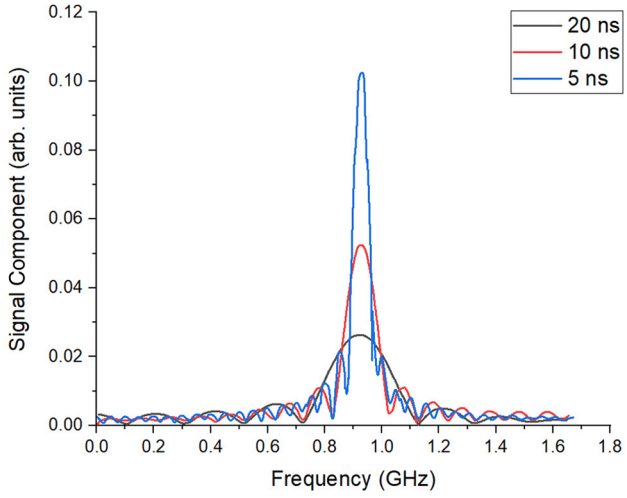

FIG. 6. Calculated spectra of the single-frequency pulses with different pulse length.

Although the designed spectrometer can be connected to a fast oscilloscope for data acquisition, the requirements for such a scope are very demanding and the costs are high. Also, scopes cannot provide shot-to-shot resolution for high repetition rates; for practical use, the pulse repetition rates can be as high as 1 kHz. To solve this problem, we develop electronics for data acquisition and processing.

The schematics of the developed data acquisition board is presented in Fig. 8. The prototype consists of the following modules: signal generator, analog-to-digital module, and a capture module. The high-speed digital data from the capture module is transmitted to a personal computer (PC). The analog-to-digital module is a low-power, 12-bit rf-sampling analog-to-digital converter, operating in single or dual channel regime at 6.4 or 3.2 GSPS, respectively. The converter has a buffered analog input, integrated digital downconverter with programmable numerically controlled oscillator, and decimation settings. The board has transformer-coupled analog inputs to accommodate a wide range of signal sources and frequencies. The developed electronics boards are controlled through an easy-to-use

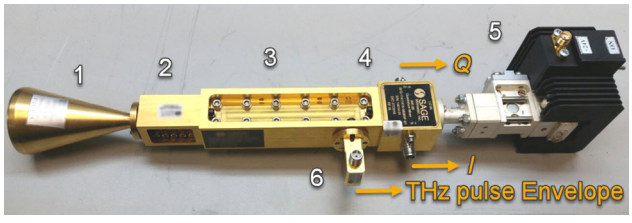

FIG. 7. Detector part of the spectrometer. 1 – 30-dB horn antenna, 2 – Band-pass filter, 3 – Directional coupler, 4 – IQ-mixer, 5 – Local oscillator, 6 – Schottky amplitude detector.

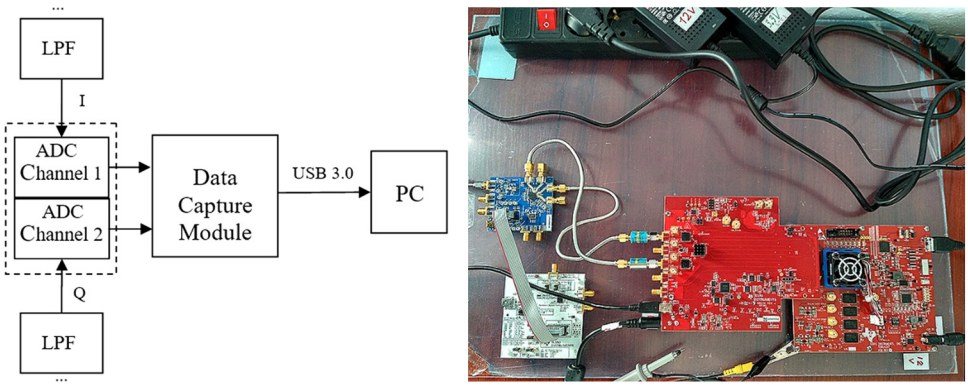

FIG. 8. The schematics (left) and the prototype (right) of the spectrometer data acquisition electronic board.

software program with a graphical user interface enabling quick configuration for a variety of uses.

The current design has the following properties:

(a) Allows quick evaluation of analog-to-digital converter (ADC) performance using Texas Instruments (TI) High-Speed Data Converter (HSDC) Pro software;

(b) Direct connection to all TI modules using an FMC+ standard [the latest standard in the FPGA Mezzanine Card (FMC)] connector (backward compatible to FMC-equipped evaluation modules);

(c) Joint Electron Device Engineering Council standard receiver and transmitter intellectual property cores with 16 routed transceiver channels and operating range from 1.6 Gbps to 15 Gbps;

(d) Onboard high-speed USB 3.0-to-parallel converter bridges the field programmable gate array (FPGA) interface to the host PC and graphical user interface;

(e) 16-Gb DDR4 synchronous dynamic random access memory (SDRAM) (split into four independent 256 × 16, 4-Gb SDRAMs; total of 1G 16-bit samples).

The board is tested with the synthesized signal of 200 MHz including the digitization and Fourier analysis (see Fig. 9). This test allows us to demonstrate a proof-of-principle of the design and evaluate the requirements of the custom-made electronics that will be built for future devices. In particular, we plan to build a custom-made board that will allow three channels, self-trigger regime, and fast shot-to-shot data acquisition and spectrometry.

IV. CHARACTERIZATION AND TESTING OF THE DEVICES

The mm-wave spectrometer and the rf switch are tested to verify their proof-of-principle operations through high-power tests with a cw 20-mW source and the MIT gyrotron. The experimental setup is shown in Fig. 5. The optical source is a 532-nm, 8-ns pulse length, Q switched laser. The laser beam is run through a beam-expanding array of lenses to prevent damage to the wafer and to illuminate more of the 100-mm diameter. We use two wafers: silicon and GaAs. Measurements of the switched

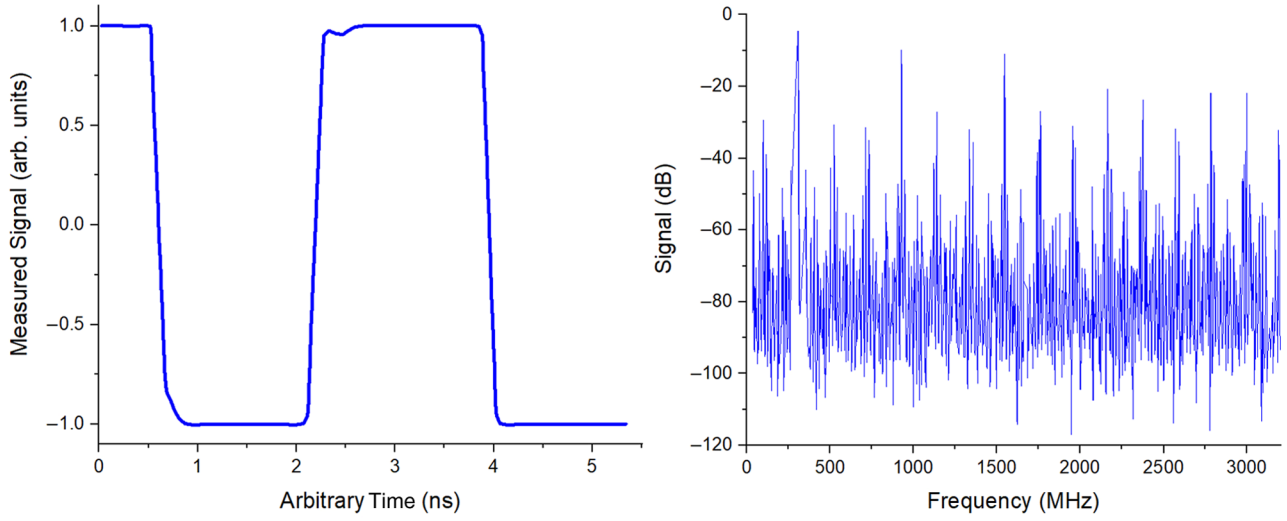

FIG. 9. Test-synthesized 200-MHz signal digitization (left) and spectroscopy (right).

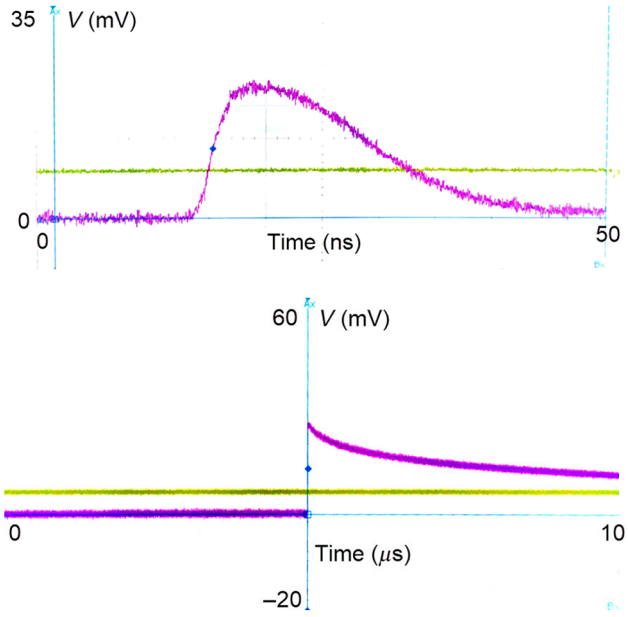

FIG. 10. Oscillograms of the reflected THz signals after laser illumination of GaAs wafer (top) and a silicon wafer (bottom) measured with the Schottky amplitude detector. Note the different time scale on the plot demonstrating the significantly slower recombination time of Si relative to GaAs.

power from the cw 110-GHz source with both wafers are shown in Fig. 10, demonstrating the orders of magnitude longer recombination time for silicon. The FWHM of the GaAs reflecting mode is about 12–15 ns, while the FWHM of the silicon is about 6 μs, 400 times longer. The rise time of both wafers is about 3 ns. Since pulse lengths of approximately 10 ns are required, the GaAs wafer is preferred for a single-wafer setup.

We also use the 20-mW cw source at 110.08 GHz to characterize the power losses inside the switch. The microwave signal power is measured with the Schottky detector in different locations of the switch components in the layout. The results of these power measurements, presented in Table I, suggest that in the current design, about half of the power is lost in the optical elements and 1/3 of the microwave power is lost on (transmitted through) the wafer and not reflected.

TABLE I. Signal power measured in different locations of the switch component layout.

Location	Schottky (mV)	Power (%)
Power source	220	100
Input window	209	95
Polarizer	182	82
Lens 1	210	95
Wafer (Cu)	135	61
Output window (Si)	50	22
Output window (Cu)	72	32

We then measure the power transmission of the switch as a function of laser beam parameters (laser pulse energy and beam spot size on the wafer) to understand the cause of power losses due to the wafers. The results of these measurements are shown in Fig. 11 and suggest that although we have enough laser power (the signal nearly saturates), we could use a larger beam spot at the wafer. We also image the laser beam spot profile on the wafer (Fig. 12), which demonstrates some irregularities in laser intensity distribution that may also contribute to the transmission reduction.

Although the transmitted power is more than sufficient to achieve the required cavity gradients of 200 MV/m, in future applications, the losses can be reduced by improving the laser beam expander optics and replacing the lossy THz lenses with gold-plated off-axis parabolic mirrors.

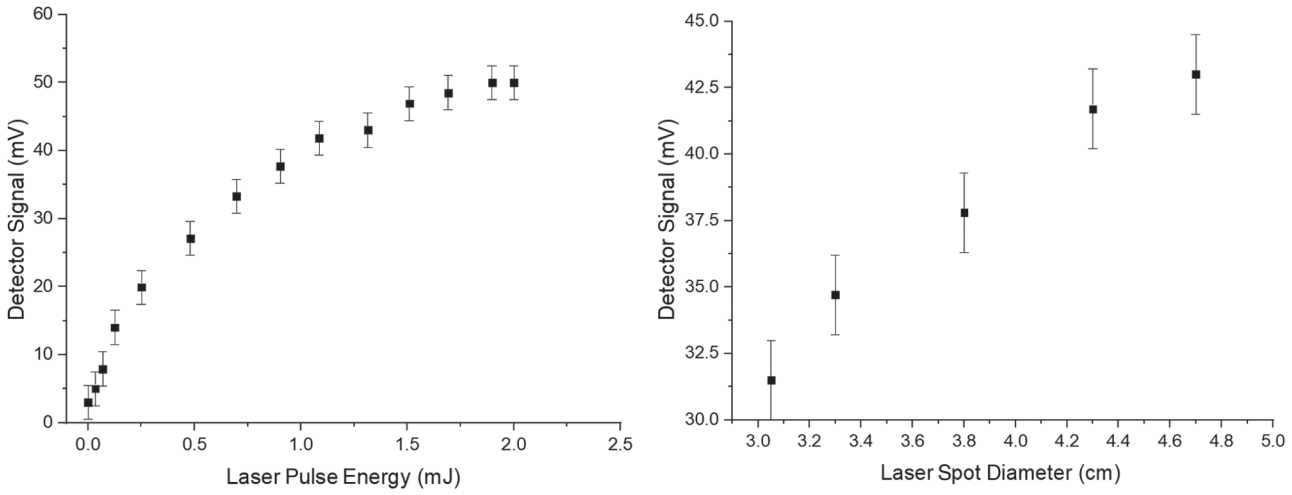

FIG. 11. Transmitted signal measured by Schottky detector as a function of laser pulse energy using the maximum spot size of 4.7 cm (left) and as a function wafer spot diameter (right).

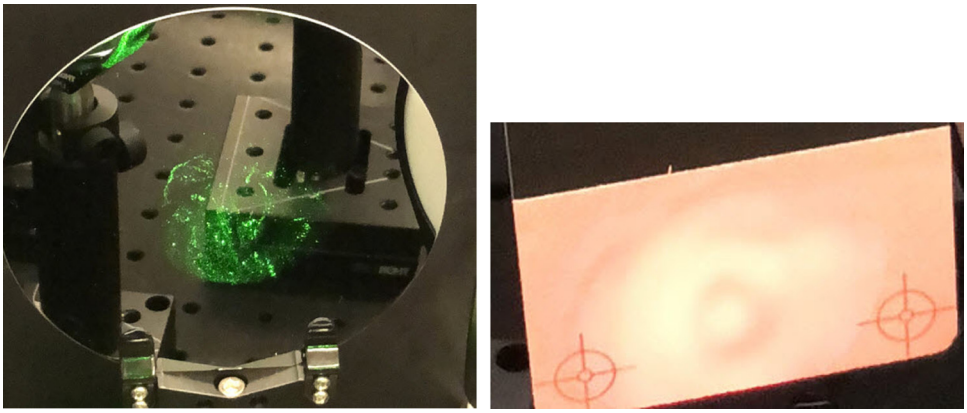

FIG. 12. Laser beam spot profile measured at the wafer (left – as is, right – with a detector card).

In high repetition and high average power applications, it is especially important to induce very high reflectivity to eliminate absorption and heating in the semiconductor switch.

After the switch is tested and characterized with the low-power source, it is shipped to the laboratory of Plasma Science and Fusion Center (PSFC) MIT to test its high-power performance with the gyrotron. The gyrotron in its current configuration produces a 3-μs pulse of 110-GHz microwaves. The maximum output power is 1.1 MW. The gyrotron output coupler produces a HE_{11} mode in the output corrugated waveguide. This mode then couples with 98% efficiency into a free space Gaussian beam with a 10.15-mm beam waist [21]. The nominal performance parameters for the gyrotron are listed in Table II [12]. The gyrotron has two high-power operating points, which can produce MW pulses. During this experimental stage, the operating parameters of the gyrotron are set for the nominal 110.08-GHz frequency. The experimental set up of this test is shown in Fig. 13.

We gradually increase the microwave power from 0 to 600 kW. The gyrotron power limit of 600 kW is due to reflections from the device under test. We measure the switch output signal with the Schottky detector and spectrometer. The test is performed with undoped Si and GaAs wafers with identical laser and THz parameters and is shown in Fig. 14. Our measurement shows that the reflectivity induced in the Si wafer is more sensitive to the laser power than the GaAs wafer and qualitatively agrees with the right plot of Fig. 4. Stable operation with each wafer at 550 kW is reached. This power will produce an accelerating gradient above 200 MV/m in a SLAC W band accelerating structure [7], including the losses from the switch components.

TABLE II. MIT gyrotron nominal operating conditions.

Nominal Frequency (GHz)	110.08
Peak Power (MW)	1.5
Pulse Length (μs)	0.1–3
Bandwidth (GHz)	+ 0.6
Rise Time (ns)	100

Finally, we check the rf breakdown detection capabilities of our spectrometer. The breakdowns that are witnessed are not normal operation or inherent to the gyrotron. The gyrotron is output coupled to a 31-mm corrugated waveguide. A mirror is required on the output of this waveguide in order to locate the rf switch enclosure within the space available in the lab.

When the rf reflects at a 90° angle, there is an enhancement of the electric field in certain regions up to a factor of 2 above the incident E field intensity, similar to that shown in Fig. 1, right. The power is high enough from the gyrotron that with that factor of 2, it reaches the air-breakdown limit. When this happens, the microwaves are scattered and reflected back toward the gyrotron, which

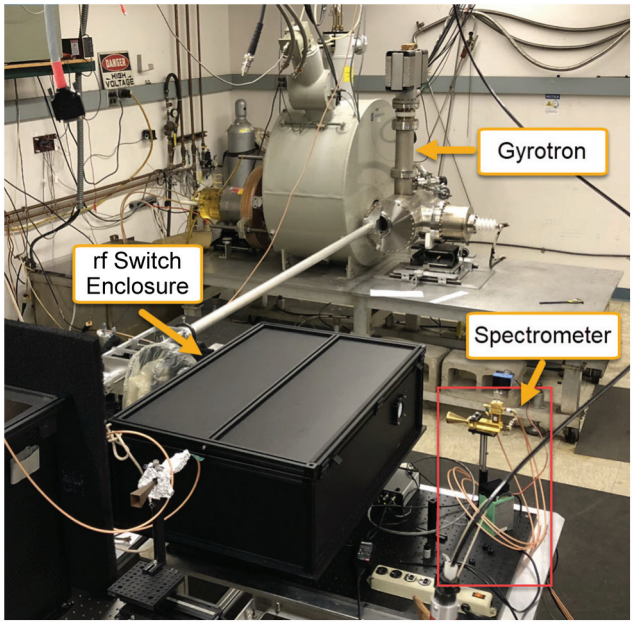

FIG. 13. The experimental set up of the high-power tests of the laser-gated rf switch at MIT PSFC lab.

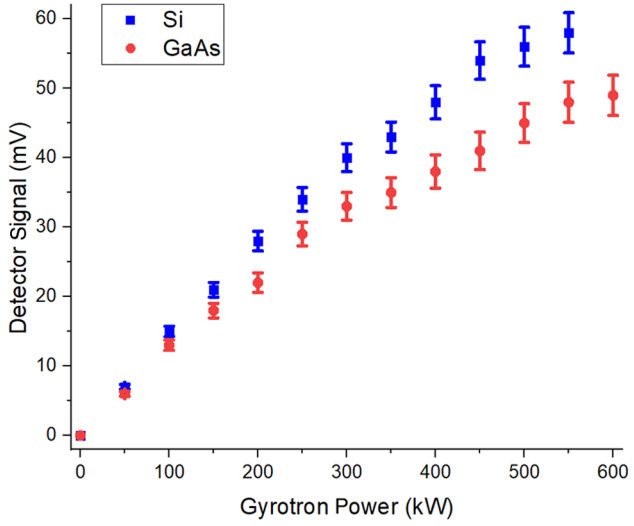

FIG. 14. Measured peak amplitude at the output of the switch as a function of gyrotron power. The vertical lines correspond to accelerating gradients of 100 and 200 MV/m in the SLAC mm-wave accelerating structure.

causes the output signal to be truncated. Each breakdown event is accompanied by the loud "bang" sound.

To register the breakdown, we put a copper disk in place of the semiconductor wafer in order to measure the full pulse length from the gyrotron. When breakdown occurs, the pulse length is shortened, while the frequency spectrum becomes wider as shown in Fig. 15. We make shot-to-shot measurements over the 500 pulses at a 1-Hz repetition rate. Pulse width, frequency bandwidth (FWHM), and shot-to-shot spectra are measured and are shown in Fig. 16, which clearly demonstrates the capability of the spectrometer to detect rf breakdown events. The spikes are clearly seen in both pulse and spectrum width measurements.

A. Summary

Future accelerators for high-energy particle physics and x-ray sources for biological and material research require miniaturized linacs. Development of compact mm-wave linacs will be advantageous in reducing the cost of future accelerator facilities. One issue in making such accelerators practical is the availability of a method to feed mm-wave rf power into these linacs. Currently, there are no mm-wave megawatt sources with nanosecond pulse lengths. Another issue is the absence of a method that reliably detects rf breakdowns, which damage the accelerating structures and interrupts their operation.

To solve these issues, we develop a laser-based rf switch and a high-resolution shot-to-shot rf spectrometer. The

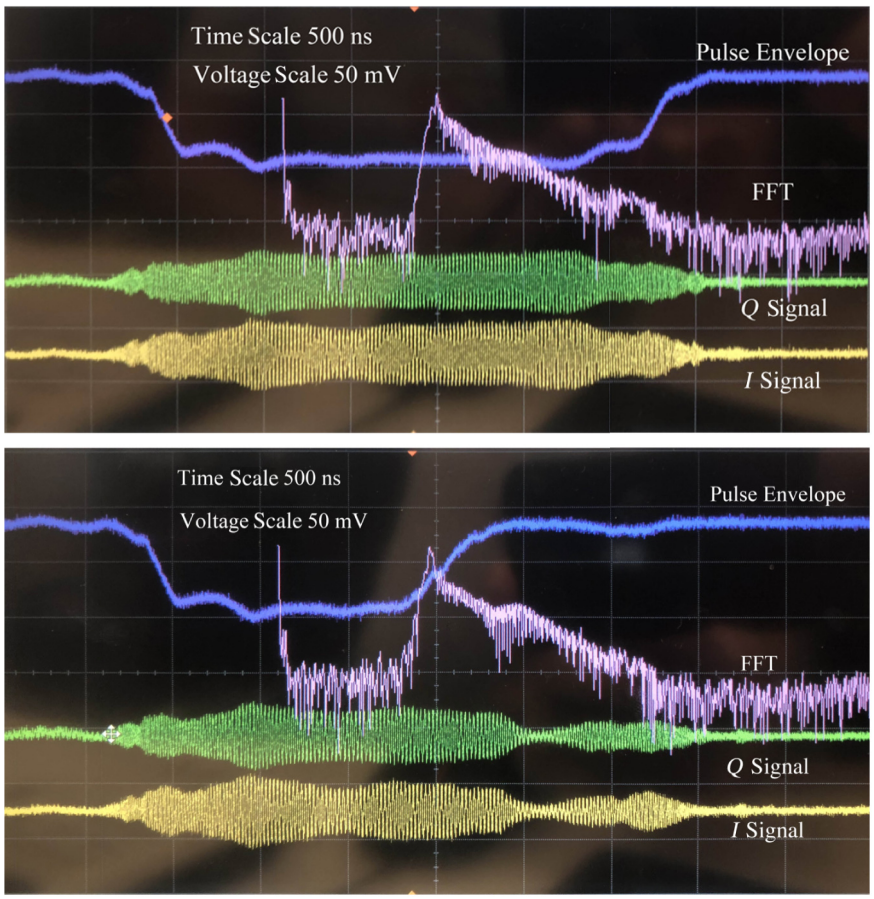

FIG. 15. Scope traces of envelopes for nonbreakdown (top) and breakdown (bottom) shots. The plot represents the following traces: blue – pulse envelope, yellow – I signal, green – Q signal, pink – FFT of I signal. Time scale of the traces is 500 ns, and voltage scale is 50 mV for I and Q signals, and 10 mV for the envelope.

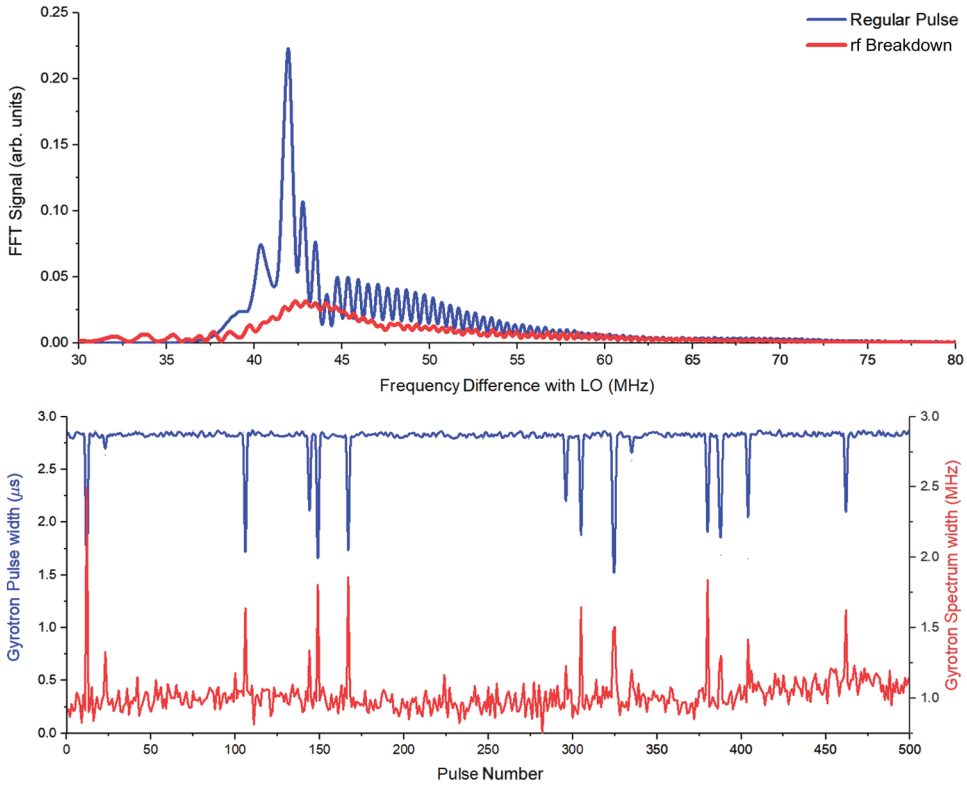

FIG. 16. Measured THz signal parameters. Top: single pulse spectra during regular (blue) and rf breakdown (red) events. Bottom: Pulse length (blue) and frequency spectrum FWHM width (red) of 500 consecutive rf pulses. Drops in pulse lengths and spikes in spectra represent breakdown events.

switch allows selecting approximately 10 ns long pulses out of microseconds long pulses, thus enabling the use of the gyrotrons as the rf source for mm-wave high-gradient linacs. The spectrometer is capable of reliably measuring nanosecond-long rf pulses, which is required to detect rf breakdowns.

We build and test prototypes of both devices. The tests demonstrate the purity of the reflected pulse without any reflection during the "off" state, rf power modulation up to 550 kW by the switch, and shot-to-shot measurements of 110-GHz pulses by the spectrometer. We demonstrate that our spectrometer reliably detect rf breakdowns of gyrotron pulse. The switch and spectrometer will allow advancement of compact mm-wave linacs, enabling miniaturization of many future accelerator facilities. In addition to the applications for accelerators, these devices will find multiple applications in the broader field of THz technology and diagnostics, as well as in *W* band power multipliers for military and telecommunication applications.

ACKNOWLEDGMENTS

This work was supported by the U.S. Department of Energy, Office of High Energy Physics, under SBIR Grant No. DE-SC0013684. The work at MIT was supported by the Department of Energy, Office of High Energy Physics, Grant No. DE-SC0015566 and Office of Fusion Energy Sciences, Grant No. DE-FC02-93ER54186.

[1] G. L. Carr, M. C. Martin, W. R. McKinney, K. Jordan, G. R. Neil, and G. P. Williams, High-power terahertz radiation from relativistic electrons, Nature **420**, 153 (2002).

[2] R. Temkin and M. Shapiro, US Workshop on High Gradient Research for Multi TeV Linear Colliders (2005).

[3] A. J. Huber, F. Keilmann, J. Wittborn, J. Aizpurua‖, and R. Hillenbrand, Terahertz near-field nanoscopy of mobile carriers in single semiconductor nanodevices, Nano Lett. **8**, 11 (2008).

[4] S. Wang and X.-C. Zhang, Pulsed terahertz tomography, J. Phys. D: Appl. Phys. **37**, 4 (2004).

[5] L. Linssen, A. Miyamoto, M. Stanitzki, and H. Weerts, Physics and Detectors at CLIC: CLIC Conceptual Design Report, *CERN Yellow Report* CERN-2012-003 (2012).

[6] M. Aicheler, P. Burrows, M. Draper, T. Garvey, P. Lebrun, K. Peach, N. Phinney, H. Schmickler, D. Schulte, and N. Toge, A Multi-TeV Linear Collider Based on CLIC Technology: CLIC Conceptual Design Report, *CERN Yellow Report* CERN-2012-007 (2012).

[7] M. Dal Forno, V. Dolgashev, G. Bowde, C. Clarke, M. Hogan, D. McCormick, A. Novokhatski, B. Spataro, S. Weathersby, and S. G. Tantawi, RF breakdown tests of mm-wave metallic accelerating structures, *Phys. Rev. Accel. Beams* **19**, 011301 (2016).

[8] M. Dal Forno, V. Dolgashev, G. Bowden, C. Clarke, M. Hogan, D. McCormick, A. Novokhatski, B. O'Shea, B. Spataro, S. Weathersby, and S. G. Tantawi, RF breakdown measurements in electron beam driven 200 GHz copper and copper-silver accelerating structures, Phys. Rev. Accel. Beams **19**, 111301 (2016).

[9] E. Nanni, V. Dolgashev, A. Haase, J. Neilson, S. Tantawi, S. Jawla, S. C. Schaub, R. J. Temkin, and B. Spataro, in *Proceedings of 9th International Particle Accelerator Conference*, Vancouver, Canada, (2018), p. 1224.

[10] E. Nanni, S. Shaub, M. Othman, V. Dolgashev, R. Li, M. C. Hoffmann, X. Wang, R. Temkin, B. Spataro, S. Tantawi, A. Haase, S. Jawla, J. Neilson, Jeffrey, and J. Picard, in *Proceedings of 18th Advanced Accelerator Concepts Workshop*, Breckenridge, CO (2018) [in the process of being published].

[11] M. Dal Forno, V. Dolgashev, G. Bowden, C. Clarke, M. Hogan, D. McCormick, A. Novokhatski, B. O'Shea, B. Spataro, S. Weathersby, and S. G. Tantawi, High gradient tests of metallic mm-wave accelerating structures, Nucl. Instrum. Methods Phys. Res A **864**, 12 (2017).

[12] E. M. Choi, C. Marchewka, I. Mastovsky, M. A. Shapiro, J. R. Sirigiri, and R. J. Temkin, Megawatt power level 120 GHz gyrotrons for ITER start-up, J. Phys.: Conf. Ser. **25**, 1 (2005).

[13] E. I. Simakov, V. A. Dolgashev, and S. G. Tantawi, Advances in high gradient normal conducting accelerator structures, Nucl. Instrum. Methods Phys. Res A **907**, 221 (2018).

[14] S. Mitsudo, T. Furuya, Y. Shimoyama, T. Fujita, Y. Tatematsu, T. Idehara, and T. Saito, in *Proceedings of 34th International Conference on Infrared, Millimeter, and Terahertz Waves*, Busan, South Korea (2009).

[15] A. Rosen, P. Stabile, W. Janton, A. Gombar, J. Delmaster, P. Basile, and R. Hurwitz, Optically controlled subsystems at HF and at mm-wavelengths, Microw. Opt. Technol. Lett. **2**, 11 (1989).

[16] L. I. Glazman, Resonant excitation of carriers in a semiconductor by a high-power light pulse, Sov. Phys. JETP **53**, 1 (1981).

[17] D. Brewster, On the laws which regulate the polarization of light by reflection from transparent bodies, Philos. Trans. R. Soc. Lond. **105**, 125 (1815).

[18] A. Beer, Bestimmung der Absorption des rothen Lichts in farbigen Flüssigkeiten, Ann. Phys. Chem. **86**, 78 (1852). [in German].

[19] M. E. Levinshtein, S. L. Rumyantsev, *Handbook Series on Semiconductor Parameters* (World Scientific, London, 1996), vol. 1, pp. 77–103.

[20] L. Rosenfeld, *Theory of Electrons* (Dover Publications, New York, 1965), p.68.

[21] J. M. Neilson, R. L. Ives, S. C. Schaub, W. C. Guss, G. Rosenzweig, R. J. Temkin, and P. Borchard, Design and high-power test of an internal coupler to HE11Mode in corrugated waveguide for high-power gyrotrons, IEEE Trans. Electron Devices **65**, 6 (2018).